New insights into the structure, chemistry, and properties of Cu_4SnS_4

Amitava Choudhury[a,*], Sudip Mohapatra[a], Hooman Yaghoobnejad Asl[a], Seng Huat Lee[b], Yew San Hor[b], Julia E. Medvedeva[b], Devon L. McClane[c], Gregory E. Hilmas[c], Michael A. McGuire[d], Andrew F. May[d], Hsin Wang[d], Shreeram Dash[e], Aaron Welton[e], Punit Boolchand[e], Kasey P. Devlin[f], Jennifer Aitken[f], Regine Herbst-Irmer[g], Václav Petříček[h]

[a] Department of Chemistry, Missouri University of Science and Technology, Rolla, MO 65409-0010, United States
[b] Department of Physics, Missouri University of Science and Technology, Rolla, MO 65409-0010, United States
[c] Department of Materials Science and Engineering, Missouri University of Science and Technology, Rolla, MO 65409-0010, United States
[d] Materials Science and Technology Division, Oak Ridge National Laboratory, Oak Ridge, TN 37831, United States
[e] Department of Electrical and Computer Science Engineering, University of Cincinnati, Cincinnati, OH 45221-0012, United States
[f] Department of Chemistry and Biochemistry, Duquesne University, Pittsburgh, PA 15282, United States
[g] Institut für Anorganische Chemie, Universität Göttingen, Göttingen, Tammannstr. 4, 37077 Göttingen, Germany
[h] Institute of Physics, Czech Academy of Sciences, Na Slovance 2, 182 21 Prague, Czech Republic

ARTICLE INFO

ABSTRACT

The ambient temperature structure of Cu_4SnS_4 has been revisited and the recently reported low temperature structure has been confirmed from single-crystal X-ray diffraction data. A structural phase transition from a large monoclinic unit cell at low temperature to a smaller orthorhombic unit cell at high temperature has been observed. The room temperature phase exhibited disorder in the two copper sites, which is a different finding from earlier reports. The low temperature monoclinic form crystallizes in $P2_1/c$ space group, which is isostructural with Cu_4GeS_4. The phase transition has also been studied with variable temperature powder X-ray diffraction and ^{119}Sn Mössbauer spectroscopy. The Seebeck coefficients and electrical resistivity of polycrystalline Cu_4SnS_4 are reported from 16 to 400 K on hot pressed pellets. Thermal conductivity measurements at high temperatures, 350 – 750 K exhibited very low thermal conductivities in the range 0.28 – 0.35 W K^{-1} m^{-1}. In all the transport measurements the phase transition has been observed at around 232 K. Resistivity decreases, while Seebeck coefficient increases after the phase transition during warming up from low to high temperatures. This change in resistivity has been correlated with the results of first-principles electronic band structure calculations using highly-accurate screened-exchange local density approximation. It was found that both the low hole effective mass of 0.63 m_e for the $\Gamma{\to}Y$ crystallographic direction and small band gap, 0.49 eV, are likely to contribute to the observed higher conductivity of the orthorhombic phase. Cu_4SnS_4 is also electrochemically active and shows reversible reaction with lithium between 1.7 and 3.5 volts.

1. Introduction

Recently there has been a tremendous surge in the Cu-based chalcogenide materials for thermoelectric [1–13] and photo-voltaic applications [14–18]. Especially interesting is the ternary and quaternary systems with diamond-like lattice exhibiting promising thermoelectric properties [1–8,10,11]. These materials show relatively high thermoelectric figure of merit value, zT, due to low thermal conductivity and tunable electronic properties. For example, high zT values have been found in the ternary compositions, $Cu^IA^{III}Te_2$ (A = In, Ga) [7,8] and Cu_2BSe_3 (B = Sn, Ge) [4,5] as well as in the quaternary compositions, Cu_2MBSe_4 (M = Zn, Cd) [1–3]. Appropriate band gap, high natural

abundance, and low cost of Cu, Sn, Zn, and chalcogen elements (S and Se) have also made them very attractive candidates for photovoltaic applications. Thus quaternary stannite structure with composition Cu_2ZnSnQ_4 (Q = S, Se, CZTS and CZTSe) [14,18–24] are being extensively studied currently as an alternative photovoltaic material in place of expensive Ga and In containing ternary or pseudo quaternary phases, $CuIn_xGa_{1-x}Se_2$ (CIGS) [25,26]. Focus has also shifted towards some of the ternary chalcogenide compositions of Cu and Sn, for example Cu_2SnQ_3 (Q = S, Se), because of the simplicity of composition and ease of solution processability in nanometric dimension for solar cell applications [15,27–33]. Efforts are also underway to discover new phases in the Cu containing chalcogenides and test their applicability in thermoelectric

devices and photovoltaic applications [34]. In this regard one of the ternary copper tin sulfide semiconductor with composition, Cu_4SnS_4, is emerging with considerable interest in thermoelectrics [35–40] and to some extent in photovoltaics [41] because of its low thermal conductivity and appropriate band gap. The interest in this compound began in 1974 since the publications by Khanafer *et al* on the structure determination and observation of a phase transition in differential scanning calorimetry as well as in electrical resistivity measurements [42,43]. Following these reports a series of investigations were initiated to study the effect of pressure and chemical substitution in anion and cations sites [44–49]. The room temperature structure was solved in orthorhombic system in *Pnma* space group [50] and phase transition was considered as dilatation with just change in the lattice parameters [42–49] or a displacive type with change in the space group as evident from the superlattice reflections in electron microscopic experiments below the transition [51]. Recently, first principles calculations were used to describe the band structure of room temperature orthorhombic and the low temperature phase, presumed to be monoclinic (Cu_4GeS_4 structure type) [52] and subsequently it was also shown from the synchrotron data that low temperature phase can be refined in monoclinic, $P2_1/c$ [40].

In this manuscript we have revisited the crystal structure of Cu_4SnS_4 at room temperature and as well as at low temperature employing single-crystal X-ray diffraction and reinforced some of the recent findings from powder X-ray diffraction data [40]. Variable temperature powder X-ray diffraction has been performed for the first time to observe the phase transition directly. In our study we have also correlated the two structures with their electronic properties through more accurate band structure calculations in the light of newly refined single-crystal atomic coordinates. Theoretical band gap has been correlated with the experimental band gap obtained from the diffuse reflectance spectra. ^{119}Sn Mössbauer spectroscopy has been carried out above and below the transition to understand the change in local environment of Sn site(s). Electrochemical lithium reaction has been carried out with Cu_4SnS_4 in order to explore its suitability as electrode material. In this article, we also report thermal transport properties of Cu_4SnS_4, especially above room temperature up to 750 K, which was not reported earlier.

2. Experimental section

2.1. Synthesis

The compound, Cu_4SnS_4, **I**, was synthesized from the stoichiometric mixture of the elements, Cu (powder, −150 mesh, 99.5%, Alfa Aesar), Sn (powder, −100 mesh, 99.5%, Alfa Aesar), and S (flakes, 99.99%, Sigma-Aldrich). All the elements were loaded in a fused quartz ampoule inside N_2-filled glove box. The ampoule was then taken out from the glove-box with the help of an adapter and hooked up in a schlenk line, evacuated, flame-sealed, and placed in a temperature-controlled furnace. The furnace temperature was increased to 450 °C at a slow rate of 3 °C/h to avoid building up of excess sulfur vapor pressure and held constant at 450 °C for 72 h. After that the temperature of the furnace was further raised to 850 °C, held constant at that temperature for another 72 h, slowly cooled to 600 °C, held there for an hour and finally decreased to room temperature at a rate of 200 °C/h. The as-synthesized product contained an ingot and on the surface of which was embedded diamond shaped crystals. These crystals were appropriate for single-crystal structure determination. After selecting few good quality single-crystals the sample was ground into fine powder for further characterization.

2.2. X-ray structure determination

The crystal structure of Cu_4SnS_4 was solved from single-crystal intensity data sets collected on a Bruker Smart Apex diffractometer with monochromated Mo Kα radiation (λ = 0.7107 Å). The data sets were collected at room temperature, 296 K and at low temperature, 170 K, using SMART [53] software employing a scan of 0.3° in ω with an exposure time of 20 s/frame, the cell refinement and data reduction were carried out with SAINT [54], the program SADABS [54] was used for the absorption correction of room temperature data, while the HABITUS was used for the numerical absorption correction of the low temperature data [55]. The structure was solved by direct method using SHELX-97 [56] and difference Fourier syntheses. Full-matrix least-square refinement against $|F^2|$ was carried out using the SHELXTL-PLUS [56] suite of programs. Structure of the title compound was solved from both the room and low temperature data in orthorhombic, *Pnma* and monoclinic, $P2_1/c$ space groups, respectively, clearly establishing the validity of structural phase transition. The room temperature structure was reported previously in *Pnma* (No. = 62) space group, however, there exist subtle differences in the two room temperature solutions with respect to the position of copper atoms (discussed later).

In the room temperature data one tin, three copper and three sulfur atoms were easily located in the Fourier maps, while subsequent refinement indicated substantial electron density close to (~0.6 Å) two copper atoms (Cu2 and Cu3). After anisotropic refinement these two electron density peaks, though reduced in intensity (~7 – 8 e/Å³), did not go away completely indicating disorder in these two copper sites. A close inspection of the Fourier maps in three-dimensions along *a*-, *b*-, and *c*- axis clearly indicated that the shape of electron density around Cu1 deviates from an ellipsoid but there is no split, while Cu2 shows clear split position, and Cu3 atom behaves very anharmonically, which can be described as either as a split atom or by anharmonic ADPs (Supporting information, Fig. S1) [57]. Therefore, for the final refinement, positions of Cu2 and Cu3 were split into three positions, two are related by mirror symmetry and the other located on the mirror, Cu2, Cu2A, Cu2a_i and Cu3, Cu3A, Cu3a_i, respectively, and their occupancies were hold together at 0.5 and refined freely. The last cycles of refinement for **I** included anisotropic thermal parameter refinement for all the atoms which yielded very good convergence to final weighted *R*-factor (wR_2 = 7.6%). The substantial improvement of the final R-values in the disordered (split copper atoms) model over the ordered copper sites model establishes the correctness of the current model over the previously solved structure from single-crystal data [42,50]. It is to be noted here that the recent Rietveld refinement from synchrotron powder X-ray data also indicated better convergence with split Cu3 site but Cu2 site was refined as an un-split position [40].

The same crystal when cooled to −103 °C (170 K) to check whether the copper disorder disappears, it was found that the cell parameters changed to a bigger monoclinic cell. The structure was easily solved in $P2_1/c$ space group with two tin, eight copper and eight sulfur atoms in the unit cell without any disorder in any of the copper atoms. This low temperature solution is isostructural with the Cu_4GeS_4 structure [58]. The low temperature structure was twinned similar to Cu_4GeS_4. A twin law of 0 0 1 0 −1 0 1 0 0, which was same as interchanging of *a*- and *c*-axis with the inversion of *b*-axis as in Cu_4GeS_4, was employed.

Details of the final refinements and the cell parameters for room and low temperature data of **I** are given in Table 1. The final atomic coordinates for the room and low temperature solutions of compound **I**, namely **I-RT** and **I-LT**, respectively, are given in Table 2 and the important inter-atomic distances and angles are listed in Table 3. Further details of the crystal structure investigations may be obtained from the Fachinformationszentrum Karlsruhe, 76344 Eggenstein-Leopoldshafen, Germany, (fax: (49) 7247-808-666; e-mail: crysdata@fiz.karlsruhe.de) on quoting the depository number CSD-432660 (RT-Cu_4SnS_4) and CSD-432661 (LT-Cu_4SnS_4).

2.3. Variable temperature powder X-ray diffraction

The room temperature and the temperature dependent powder X-ray diffraction scans from 300 K down to 20 K in 20 K increments were

Table 1

Crystal data and structural refinement parameters for compound **I** at room and low temperature.

Compound	I-RT	I-LT
Empirical formula	Cu_4SnS_4	Cu_4SnS_4
Formula weight	501.09	501.09
Temperature/K	296(2)	170(2)
Wavelength/Å	0.71073	0.71073
Crystal system, space group	Orthorhombic, *Pnma*	Monoclinic, *P2$_1$/c*
Unit cell dimensions	a = 13.566(2) Å	a = 10.058(6)Å
	b = 7.689(3)Å	b = 13.489(8)Å
	c = 6.416(2)Å	c = 10.085(6)Å
	β = 90°	β = 100.840°
Volume/Å^3	669.38(16)	1343.8(13)
Z, Calculated density	4, 4.972 Mg/m^3	8, 4.953 Mg/m^3
Absorption coefficient	17.304 mm^{-1}	17.239 mm^{-1}
F(000)	920	1840
Limiting indices	−17 < = h < = 18, −10 < = k < = 10, −8 < = l < = 8	−13 < =h < =13, −17 < =k < =17, −13 < =l < =13
Reflections collected / unique	7819 / 893 [R(int) = 0.0272]	15860 / 3314 [R(int) = 0.1642]
Refinement method	Full-matrix least-squares on F^2	Full-matrix least-squares on F^2
Data / restraints / parameters	893 / 14 / 71	3314 / 0 / 164
Goodness-of-fit on F^2	1.081	0.967
Final R indices [I > 2σ(I)]	R$_1$ = 0.0319[a], wR$_2$ = 0.0753[b]	R1 = 0.0672[a], wR2 = 0.1277[b]
R indices (all data)	R$_1$ = 0.0346, wR$_2$ = 0.0768	R1 = 0.1149, wR2 = 0.1461
Largest diff. peak and hole	1.794 and −1.454 e.A^{-3}	2.132 and −2.157 e.A^{-3}

[a] $R_1 = \Sigma \, ||Fo|-|Fc||/ \Sigma \, |Fo|$.

[b] $wR_2 = \{\Sigma \, [w(F_O^2 - F_c^2)^2] / \Sigma \, [w(F_O^2)^2]\}^{1/2}$, $w = 1/[\sigma^2(F_O) + (aP)^2+bP]$ where $P = [F_O^2 + 2F_C^2]/3$; a = 0.0298 and b = 7.6691 for **I-RT** and a = 0.0449 and b = 0.0000 for **I-LT**.

carried out in an Oxford PheniX cryostat on a PANalytical X'Pert Pro MPD diffractometer using monochromated Cu K$_{\alpha1}$ radiation.

2.4. Sample preparation for physical property measurements

The finely ground as-synthesized samples were first checked for phase purity by employing powder X-ray diffraction. The fine powder was then subjected to hot pressing in a graphite die of 0.5 in. diameter in a graphite furnace. The temperature was slowly raised, over 30 min, to 650 °C and hot pressed at that temperature for about an hour in a high purity argon atmosphere. The pressure was withdrawn and the furnace was cooled down to room temperature over a period of one hour. This hot pressing method produced hard cylindrical disks with 95% of the crystallographic density. These disks were further polished for high-temperature thermal diffusivity measurements, and were cut into bar shaped pieces with 2 × 2 × 6 mm dimension for low temperature transport measurements limited to resistivity and Seebeck coefficient. To verify the phase purity of the hot-pressed pellet we have collected high quality laboratory powder X-ray diffraction data from the finely ground broken pieces of the pressed pellet. The Rietveld refinement of the diffraction data showed very good convergence with the theoretical pattern indicating phase purity of the sample as shown in Fig. 1.

2.5. Physical property measurements

Low temperature, 2 − 400 K, transport measurements were performed in a Quantum Design Physical Property Measurement System (PPMS). These include Seebeck coefficient (α) and electrical resistivity (ρ) measurements to investigate the change in electronic properties upon phase transition employing the PPMS thermal transport option (TTO) using the standard four-probe contact method on a 2 × 2 × 6 mm^3 sample bar. The above room temperature thermal diffusivity D_T was measured on 12.7 mm diameter disks of approximately 1.5 mm thickness in an Anter FL-5000 with a graphite furnace. Thermal

Table 2

Positional coordinates and equivalent isotropic displacement parameters for **I-RT** and **I-LT**. Ueq = 1/3rd of the trace of the orthogonalized U tensor.

	Atom	Wyck.	Occ.	x/a	y/b	z/c	U$_{eq}$ [Å^2]
I-RT							
	Sn1	4c	1	0.08679(1)	¼	0.12620(1)	0.015(1)
	Cu1	8d	1	0.33561(1)	0.98739(1)	0.12660(1)	0.040(1)
	S1	8d	1	0.17488(1)	0.00047(2)	0.26116(2)	0.017(1)
	S2	4c	1	0.08423(1)	¼	0.75042(3)	0.017(1)
	S3	4c	1	0.41914(1)	¼	0.24379(3)	0.020(1)
	Cu2	4c	0.78	0.34331(1)	¼	0.55903(3)	0.037(1)
	Cu3A	8d	0.78	0.43942(5)	0.30114(9)	0.89608(5)	0.049(2)
	Cu2A	8d	0.22	0.32055(9)	0.14398(9)	0.47385(5)	0.065(5)
	Cu3	4c	0.22	0.42021(9)	¼	0.84278(9)	0.053(5)
I-LT							
	Sn1	4e	1	0.06360(9)	0.41498(9)	0.31975(9)	0.010(1)
	Sn2	4e	1	0.55368(9)	0.08854(9)	0.30913(9)	0.010(1)
	Cu1	4e	1	0.0784(3)	0.6861(2)	0.0143(3)	0.018(1)
	Cu2	4e	1	0.1254(3)	0.05457(8)	0.4659(3)	0.020(1)
	Cu3	4e	1	0.1636(3)	0.6857(2)	0.2830(3)	0.019(1)
	Cu4	4e	1	0.1958(3)	0.15567(9)	0.1849(3)	0.018(1)
	Cu5	4e	1	0.2912(3)	0.5860(2)	0.5275(3)	0.030(1)
	Cu6	4e	1	0.3418(3)	0.35576(8)	0.0860(3)	0.019(1)
	Cu7	4e	1	0.4263(3)	0.33774(9)	0.4320(3)	0.019(1)
	Cu8	4e	1	0.6821(3)	0.3485(2)	0.1793(3)	0.019(1)
	S1	4e	1	0.0091(6)	0.0798(4)	0.2543(5)	0.011(1)
	S2	4e	1	0.1226(6)	0.3232(4)	0.1300(5)	0.011(1)
	S3	4e	1	0.1351(6)	0.8290(4)	0.1330(5)	0.012(1)
	S4	4e	1	0.2531(6)	0.4197(4)	0.5031(5)	0.011(1)
	S5	4e	1	0.2539(5)	0.5829(4)	0.0029(5)	0.013(1)
	S6	4e	1	0.3662(5)	0.1759(4)	0.3721(5)	0.012(1)
	S7	4e	1	0.5011(6)	0.4187(4)	0.2561(5)	0.014(1)
	S8	4e	1	0.6117(6)	0.1802(4)	0.1192(5)	0.014(1)

Table 3
Selected bond distances and angles for the coordination polyhedra of **I-RT** and **I-LT**.[a]

I-RT		I-LT			
Atom − atom	Distances (Å)	Atom − atom	Distances (Å)	Atom − atom	Distances (Å)
	Sn − S			Sn − S	
Sn1—S2[#1]	2.4116(8)	Sn1—S4	2.394(5)	Sn2—S6	2.408(6)
Sn1—S1[#2]	2.4206(9)	Sn1—S1[i]	2.415(5)	Sn2—S7[iii]	2.418(5)
Sn1—S1	2.4206(9)	Sn1—S3[ii]	2.434(6)	Sn2—S8	2.441(6)
Sn1—S3[#3]	2.4227(9)	Sn1—S2	2.444(6)	Sn2—S5[iii]	2.443(5)
	Cu − S			Cu − S	
Cu1—S2[#4]	2.2685(8)	Cu1—S2[iv]	2.261(6)	Cu6—S6[vii]	2.257(6)
Cu1—S1[#5]	2.3474(8)	Cu1—S5	2.268(6)	Cu6—S7	2.279(5)
Cu1—S1[#4]	2.3512(9)	Cu1—S3	2.284(6)	Cu6—S2	2.370(6)
Cu1—S3[#5]	2.4345(9)	Cu2—S5[v]	2.251(6)	Cu7—S4	2.289(7)
Cu2—S1[#10]	2.3350(9)	Cu2—S1	2.258(5)	Cu7—S6	2.315(6)
Cu2—S1[#11]	2.3350(9)	Cu2—S2[v]	2.340(6)	Cu7—S7	2.326(7)
Cu2—S3	2.269(2)	Cu3—S1[i]	2.226(6)	Cu7—S8[v]	2.403(6)
Cu2A—S1[#11]	2.153(9)	Cu3—S8[vi]	2.291(6)	Cu8—S5[x]	2.257(7)
Cu2A—S1[#8]	2.153(9)	Cu3—S3	2.438(6)	Cu8—S7	2.311(7)
Cu2A—S3	2.152(9)	Cu4—S4[vii]	2.265(6)	Cu8—S3[iii]	2.392(6)
Cu2A—S1	2.643(4)	Cu4—S6	2.315(6)	Cu8—S8	2.422(6)
Cu3—S2[#12]	2.304(9)	Cu4—S1	2.357(7)		
Cu3—S1[#11]	2.377(8)	Cu4—S2	2.408(6)		
Cu3—S1[#10]	2.377(8)	Cu5—S4	2.282(6)		
Cu3—S3[#9]	2.57(4)	Cu5—S8[vi]	2.301(7)		
Cu3A—S2[#12]	2.213(5)	Cu5—S3[viii]	2.354(7)		
Cu3A—S3[#9]	2.282(4)	Cu5—S7[ix]	2.724(6)		
Cu3A − S1[#10]	2.346(6)				
	Cu − Cu			Cu − Cu	
Cu1—Cu 2A[#5]	2.541(6)			Cu2—Cu6[v]	2.584(4)
Cu1—Cu 2A[#4]	2.543(7)			Cu3—Cu8[vi]	2.675(4)
Cu1—Cu 3A[#6]	2.611(7)			Cu1—Cu3	2.684(4)
Cu1—Cu3[#7]	2.95(2)			Cu1—Cu2[i]	2.747(4)
Cu2—Cu3A	2.556(6)			Cu3—Cu5	2.888(4)
Cu3—Cu2A[#2]	2.85(4)			Cu5—Cu7[ix]	2.977(5)
				Cu8—Cu5[ix]	3.049(5)

[a]Symmetry transformations used to generate equivalent atoms: [#1] x, y, z − 1; [#2] x, -y+1/2, z; [#3] x − ½, y, -z + ½; [#4] −x + 1/2, -y + 1, z - 1/2; [#5] x, y + 1, z; [#6] x, -y + 3/2, z − 1; [#7] x, y + 1, z − 1; [#8] −x + 1/2, -y, z - ½; [#9] x, y, z + 1; [#10] − x + 1/2 , y + 1/2, z + ½; [#11] − x + 1/2 , - y, z + ½; [#12] x + ½ , y, - z + 3/2.
[i] −x, 0.5 + y, 0.5 − z; [ii] − x, - 0.5 + y, 0.5 − z; [iii] 1 − x, - 0.5 + y, 0.5 − z; [iv] − x, 1 − y, - z; [v] x, 0.5 − y, 0.5 + z; [vi] 1 − x, 0.5 + y, 0.5 − z; [vii] x, 0.5 − y, - 0.5 + z; [viii] x, 1.5 − y, 0.5 + z; [ix] 1 − x, 1 − y, 1 − z; [x] 1 − x, 1 − y, - z.
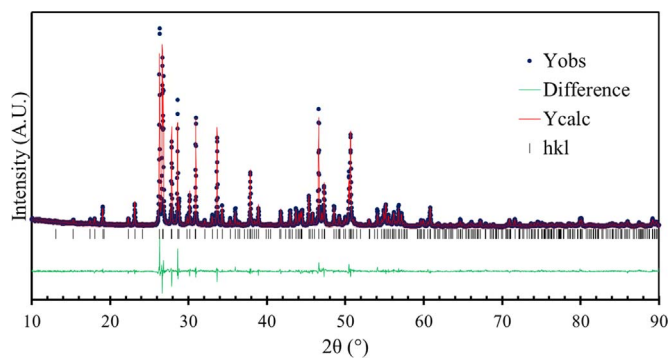

Fig. 1. Rietveld refinement of the laboratory powder X-ray diffraction data of finely ground hot-pressed pellet of Cu_4SnS_4. The weighted data residuals wR = 10.69% and unweighted phase residuals, RF^2 = 6.97%, RF = 5.37%.

conductivity data was calculated using equation, $\kappa = D_T C_P d$, where d is the density. The specific heat capacity (Cp) between room temperature and 673 K was measured employing differential scanning calorimetry (DSC) in TA instrument's Q2000 instrument, while Cp data from Anter FL-5000 instrument was used for the temperature range 673–750 K.

2.6. Diffuse reflectance UV–Vis–NIR spectroscopy

Diffuse reflectance measurements for Cu_4SnS_4 was performed on a Varian Cary 5000 UV–Vis–NIR spectrophotometer equipped with a Praying Mantis accessory. $BaSO_4$ powder (Fisher, 99.92%) was used as a 100% reflectance standard. The Kubelka–Munk function was applied to obtain band gap information [59,60].

2.7. Theoretical calculations

First-principles density-functional calculations were performed to investigate the electronic band structure of the monoclinic and orthorhombic Cu_4SnS_4. For this, highly-precise full-potential linearized augmented plane wave method [61,62] with self-consistent screened-exchange local density approximation, sX-LDA [63,64] was employed. The sX-LDA method provides a better energy functional compared to LDA or generalized gradient approximation by modeling the exchange-correlation hole within a *nonlocal* density scheme, and has been shown to successfully describe the band gaps in narrow-to-wide gap semiconductors and insulators [65–67].

For 36- and 72-atom cells of disordered orthorhombic and monoclinic Cu_4SnS_4, summations over the Brillouin zone were carried out using 10–14 special **k** points in the irreducible wedge. Cut-offs for the basis functions, 12.4 Ry, and potential representation, 81.0 Ry, and expansion in terms of spherical harmonics with $l \leq 8$ inside the muffin-tin spheres were used. For every structure investigated, the internal positions of all atoms were optimized via the total energy and atomic forces minimization.

2.8. Electrochemistry

For electrochemical studies a cathode film was prepared. In this regard the active material, Cu_4SnS_4, was first milled with super P
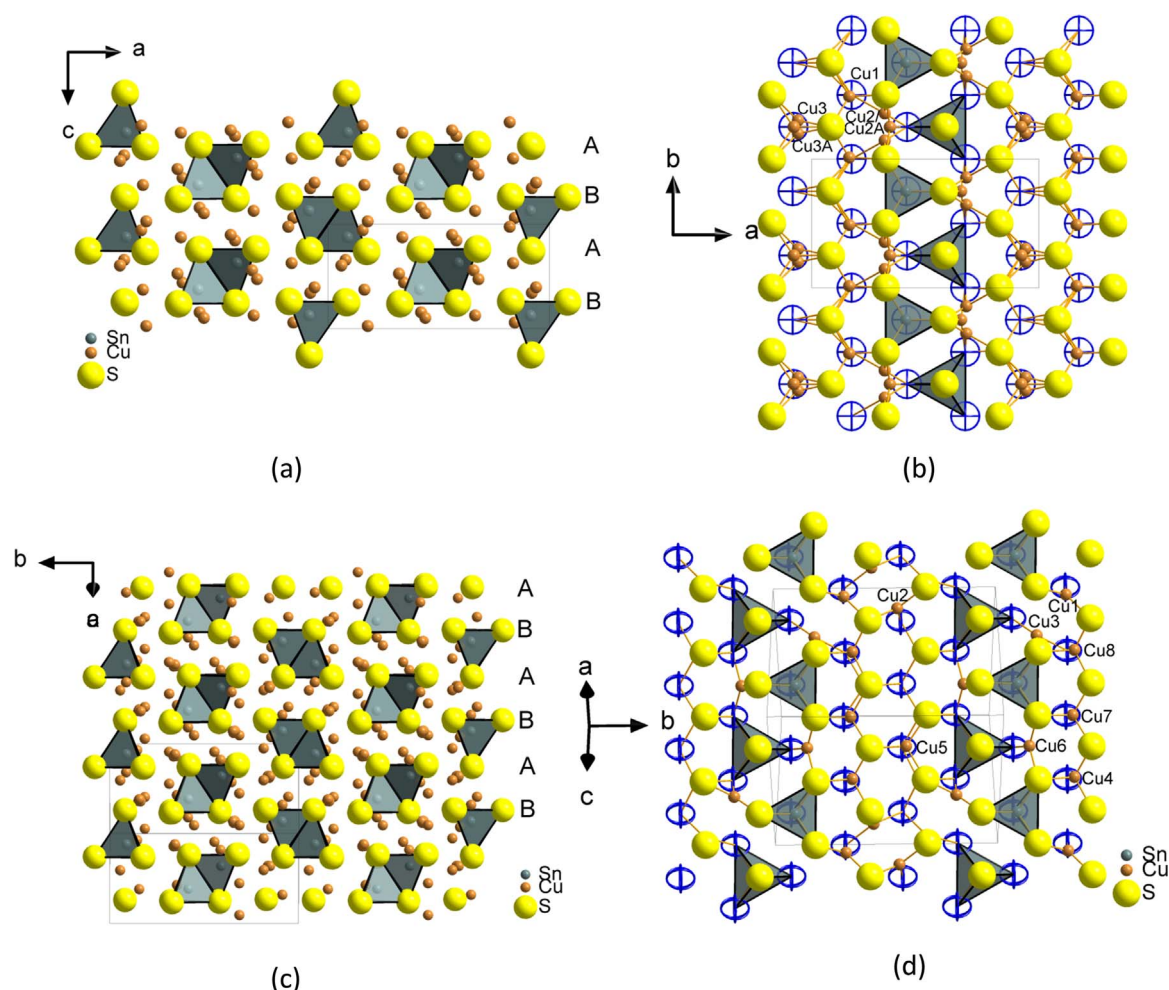
(a)

(b)

(c)

(d)

Fig. 2. (a) ABAB stacking of the close packed sulfide layers of Cu_4SnS_4 (**I-RT**) are shown with the tetrahedral interstitial holes are filled by Sn and Cu atoms. (b) Two close packed sulfide layers of Cu_4SnS_4 (**I-RT**) are viewed from top. The top layer is shown as filled yellow sphere and bottom sulfide layer is shown with blue empty circles. Sn atoms occupy the perfect tetrahedral sites, while two of the copper atoms are disordered and reside away from the center of the tetrahedral site. Note all octahedral sites are empty. (c) ABAB stacking of the sulfide layers of Cu_4SnS_4 (**I-LT**) are shown with the tetrahedral interstitial holes filled by Sn and Cu atoms. (d) Two close packed sulfide layers of Cu_4SnS_4 (**I-LT**) are viewed from top; yellow spheres top layer and blue empty circles are denoted as bottom layer. Cu1, Cu2, Cu3 and Cu6 atoms are away from the center of the tetrahedral hole and reside on the face of the tetrahedral hole with trigonal coordination. (For interpretation of the references to color in this figure legend, the reader is referred to the web version of this article.)

conductive carbon vigorously in a SPEX 8000 miller for 2 h followed by addition of Poly-vinylidene fluoride (PVDF) as binder dissolved in N-Methyl-2-pyrrolidone (NMP). The resulting mixture was further ball milled for 20 min until a homogeneous, viscous slurry was obtained. The ratio of the active material, conducting carbon, and the binder in cathode mix was 75:15:10. The cathode mix was then spread as a film of uniform thickness onto a flat sheet of carbonized aluminum current collector with a glass rod and dried in a vacuum oven for 12 h at 80 °C.

For electrochemical tests, CR2032 type coin cells were fabricated using the above composite cathode film cut into circular disks (3/8 in. diameter) with 4.5 – 5.5 mg of active material loading. The cells were assembled in an argon filled glove box with oxygen concentration below 2.0 ppm. The cathode disk and Li anode (0.75 mm thickness Li ribbon cut into circular disk) were mounted in the cell using a Celgard® 2325 circular sheet placed between the two electrodes as the separator. The electrolyte, 1 M solution of $LiPF_6$ in DMC-EC (1:1) was then added and the cell was sealed with a coin cell crimper. The prepared cells were aged for equilibration for several hours before electrochemical testing. Voltage-composition profiles were obtained using galvanostatic charge-discharge experiments done on an Arbin Instruments battery tester, model BT2043, in the potential range 1.8 – 3.5 V with a constant current charge and discharge modes at a C-rate of C/50.

2.9. Mössbauer spectra

^{119}Sn Mössbauer spectra of the powdered sample of Cu_4SnS_4 were collected at 77 and 298 K using ^{119m}Sn in $CaSnO_3$ as an emitter.

3. Results and discussion

3.1. Structure description

The room temperature structure of Cu_4SnS_4, **I-RT**, has already been described [50]. The only difference is the modeling of the disorder in two of the copper sites, which are statistically disordered between the three sites, Cu2A, Cu2, Cu2a_i and Cu3, Cu3A, Cu3a_i with i: x, 0.5-y, z, respectively. The structure of **I-RT** can be described as a 3-dimensional (3D) framework built up of SnS_4 and CuS_4 tetrahedral units and trigonal CuS_3 unit. In terms of packing, the structure can be described as approximately hexagonal packing of sulfur anions forming layers, which are stacked in *ABAB*... fashion (Fig. 2a). The octahedral holes between the layers are empty and can easily be visualized when viewed perpendicular to the *ab*-plane. Five out of eight available tetrahedral holes are filled by four Cu and one Sn atoms in which one fourth of the Cu atoms (Cu2A, Cu2, Cu2a_i) occupying tetrahedral
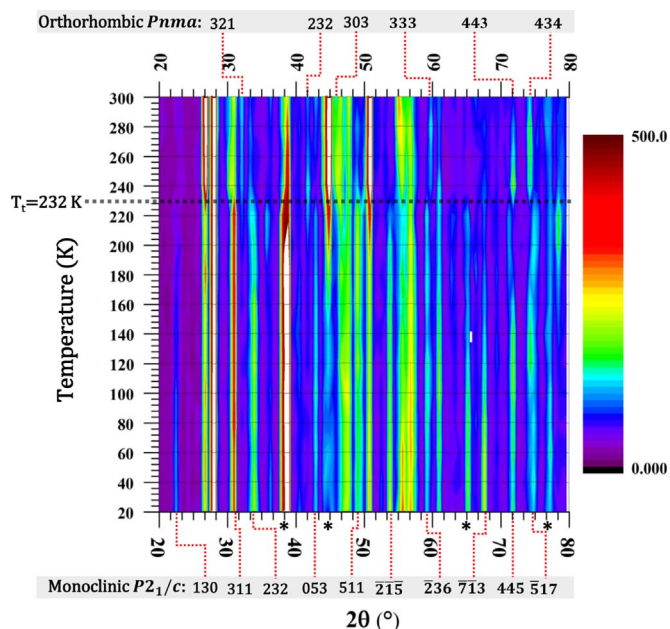
Fig. 3. Thermodiffractogram of Cu_4SnS_4. The intensities are color-coded according to the panel on the right. Asterisks indicate lines due to Al sample holder.

holes are moved towards the faces of the tetrahedron and adopt a planar triangular coordination. However, Sn1, Cu1 and disordered Cu3, Cu3A, Cu3a_i still retain their tetrahedral geometry, though Cu1 has high thermal parameters compared to Sn1 (Fig. 2b). There is a range of Cu – S distances in this compound. For Cu1, Cu – S distances range between 2.268(2) – 2.424(2) Å, while in the disordered Cu sites Cu – S distances vary between 2.153(9) – 2.643(4) Å (Table 3). Cu – S and Sn – S distances are in good agreement with the related compounds, for example, $Cu_4Sn_7S_{16}$ and Cu_2SnS_3, reported in the literature [68]. There are several Cu – Cu close contacts because of the edge-sharing between the Cu1 and Cu3/Cu3A/ Cu3a_i centered tetrahedra as well as between Cu1- centered tetrahedron and Cu2/Cu2A/Cu2a_i centered triangle.

The low temperature structure of Cu_4SnS_4, **I-LT**, is double the unit cell of **I-RT** and can be transformed from the room temperature unit cell by employing the following matrix, 0 1 1 −1 0 0 0 −1 1. The **I-LT** asymmetric unit contains two tin, eight copper, and eight sulfur atoms and is isostructural with Cu_4GeS_4 [58]. The structure of **I-LT** is built up of corner and edge-sharing between the SnS_4, CuS_4 tetrahedra and CuS_3 triangles. In terms of packing, the structure is similar to **I-RT**, where it forms hexagonal close-packed layers of sulfur anions, which stack in *ABAB...* fashion (Fig. 2c). The cations, Sn and Cu, fill the 5/8 of the available tetrahedral holes while all the octahedral holes are empty. However, unlike **I-RT**, the **I-LT** structure has 50% of the copper sites (Cu1, Cu2, Cu3, and Cu6) located in the center of a triangle as compared to 25% in the **I-RT** structure (Fig. 2d). More importantly, all the atomic positions are ordered and well-defined as reflected by their isotropic thermal parameters (Table 2).

3.2. Phase transition as observed by variable temperature powder X-ray diffraction

The variable temperature PXRD reveals the disappearance of certain diffraction lines and appearance of new lines while transitioning from the low temperature to high temperature phase. The phase transition can be clearly seen at about 232 K as the low temperature monoclinic phase specific reflections, (311), (232), (053),(511), ($2\bar{1}\bar{5}$),($\bar{2}$36), ($\bar{7}\bar{1}$3), (445) ,($\bar{5}$17) disappear and the orthorhombic phase specific reflections, (321),(232),(303),(333), (443), and (434) appear (Fig. 3).

3.3. ^{119}Sn Mössbauer experiment

To get a better insight into the change of local environment of SnS_4 tetrahedra, ^{119}Sn Mössbauer spectroscopy was carried out above (300 K) and below the transition temperature (78 K) as shown in Fig. 4. Interestingly, both isomer shift (δ) and quadrupole splitting (ΔE_Q) parameters, which yield information about the oxidation state and local symmetry of Sn, respectively, are almost identical before and after the transition (Table 4). The isomer shift values of 1.47 and 1.45 mm/s at 78 and 298 K, respectively, and quadrupole splitting value of 0.15 mm/s at both temperatures agree well with Sn in +4 oxidation state and in tetrahedral coordination with sulfur environment, for example, as in stannite structure type compounds, Cu_2FeSnS_4 or Cu_2ZnSnS_4 [69]. Though crystallographically there are two independent Sn sites in the low temperature monoclinic structure, the Mössbauer spectrum show only little broadening indicating that the SnS_4 tetrahedron remains unperturbed during the transition and it is the mobility of Cu atoms that instigate the phase transition. The fact that the ^{119}Sn Mössbauer spectra of the monoclinic and orthorhombic phases of Cu_4SnS_4 are almost identical, corroborates well with the SnS_4 tetrahedral site analysis based on the crystallographic information. The average Sn − S bond lengths in monoclinic and orthorhombic forms are 2.4245(4) and 2.4189(5) Å, respectively. This indicates that the various tin sites are experiencing the same effective environment from sulfur atoms. Moreover, the bond angle variance of 14.97^{o2} for Sn1 is considerably higher than that of Sn2 site, 6.8519^{o2} in monoclinic Cu_4SnS_4 which is almost comparable to the value of 5.8087^{o2} of Sn1 in orthorhombic form. Consequently this fact supports the observed increase in broadening of the absorption peaks in the monoclinic form. It is worth noting here that the local distortions of
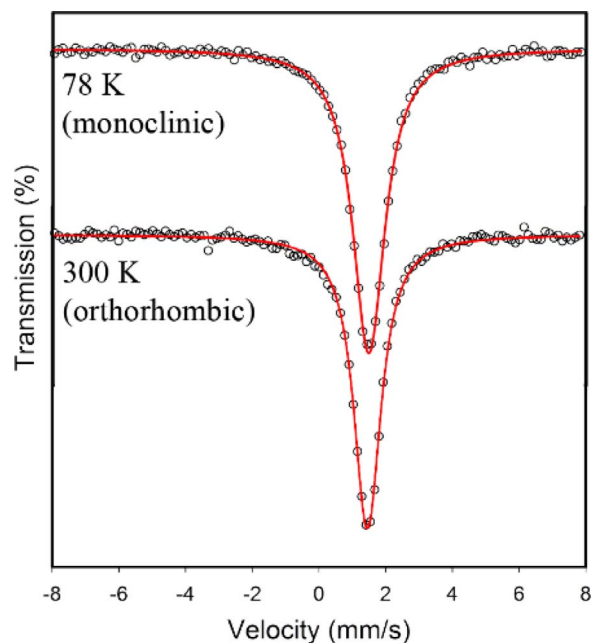

Fig. 4. ^{119}Sn Mössbauer spectra of Cu_4SnS_4 at 78 (top) and 300 K (bottom).

Table 4
The fitted ^{119}Sn Mössbauer spectroscopic values for isomer shift (δ), quadrupole splitting (ΔE_Q), and linewidth (Γ) of as-synthesized Cu_4SnS_4.

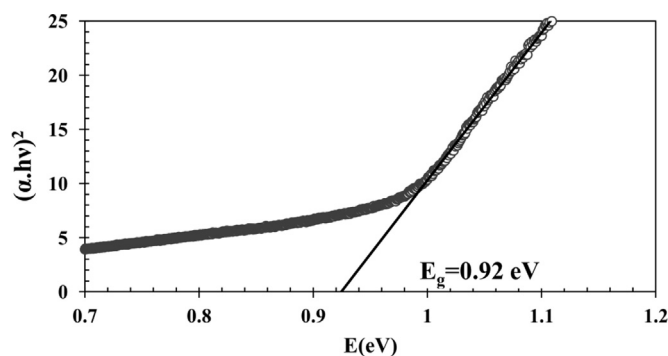| As-synthesized Cu_4SnS_4			
T/K	δ (mm/s)	ΔE_Q (mm/s)	Γ (mm/s)
78	1.477	0.15	1.113
300	1.45	0.15	0.95

Fig. 5. The diffuse reflectance plot of Cu$_4$SnS$_4$.

SnS_4 tetrahedra in orthorhombic and monoclinic forms of Cu$_4$SnS$_4$ are much less compared to many quaternary Sn – S phases. For example, in Rb$_2$Cu$_2$SnS$_4$, the Sn1 tetrahedron has an angle variance of 31.30^{o2}, while in Rb$_2$Cu$_2$Sn$_2$S$_6$, the Sn1 and Sn2 sites have bond angle variance of 44.78 and 46.24^{o2}, respectively [70]. Table S-1 (supporting information) provides the details of the tetrahedral site analysis based on crystallographic information.

3.4. Optical bandgap

The room temperature optical band gap of Cu$_4$SnS$_4$ was estimated from diffuse reflectance data. To obtain the optical gap, E_g, the equation, $\alpha h\nu = A(h\nu - E_g)^m$ (equation 1) was used, where α = absorption coefficient/Kubelka-Munk function, $h\nu$ = photon energy and A = constant, the exact value of "m" must be applied in equation 1 to determine the optical band gap and understand the nature electronic transition responsible for absorption. For example, the value of exponent, $m = \frac{1}{2}$ and 2 are applied for direct and indirect gap transition, respectively. Accordingly, the square root and the square of $h\nu\alpha$ are plotted against the photon energy and the linearity of the absorption edge is analyzed to determine the indirect and direct nature of the absorption. In this case, Cu$_4$SnS$_4$ sample exhibits linearity in $(h\nu\alpha)^2$ vs $h\nu$ plot, which suggests that the sample possesses a direct band gap of 0.92 eV (Fig. 5). This result bear close resemblance to that reported for thin film of Cu$_4$SnS$_4$ [71].

3.5. Transport properties

Fig. 6 shows the transport property measurements at low temperatures (16 – 400 K) as a function of temperature for Cu$_4$SnS$_4$ sample that include electrical resistivity and Seebeck coefficient. Fig. 6a shows that the electrical resistivity decreasing with increasing temperature
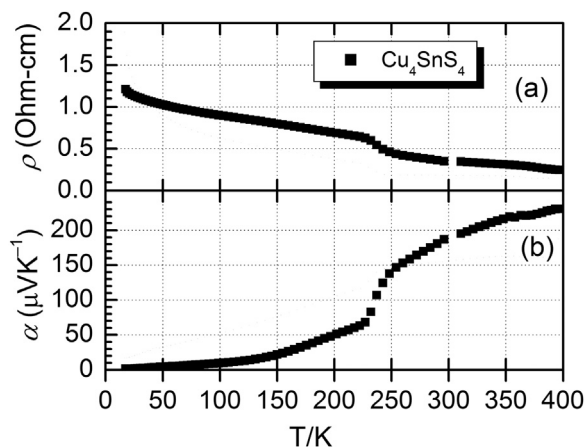
indicating semiconducting behavior. The phase transition can be seen as a jump in resistivity plot at around 232 K when the temperature is lowered. On the other hand it can be stated that the high temperature phase is more conducting. The dependence of conductivity on temperature is thermally activated and the plot of $\ln\rho$ vs. $1/T$ produced straight lines of two intersecting slopes before and after the transition (Supporting information, Fig. S2). However, fitting of the activation energy curve is poor when a wider range of temperatures is considered. Nevertheless, the sample behaved like a narrow band gap semiconductor.

Cu$_4$SnS$_4$ showed large positive Seebeck coefficients indicative of a *p*-type transport behavior. The Seebeck coefficients increase with increasing temperature as shown in Fig. 6b in the temperature range 16–400 K. The *p*-type behavior indicates that major carriers are predominantly holes possibly arising from Cu deficiency. Initially the Seebeck coefficient increases sluggishly from 1.5 μV K^{-1} at 17 K to 68 μV K^{-1} at 227 K and jumps rapidly after the phase transition and reaches a value of 146 μV K^{-1} at 253 K and continue to increase till 400 K reaching a value of 231 μV K^{-1}. The variation of Seebeck coefficient of Cu$_4$SnS$_4$ is similar to that reported by Goto et al [39].

High temperature thermal conductivity as calculated from the diffusivity data (Fig. 7a) show remarkably low values, 0.28–0.35 W m^{-1} K^{-1}, between 350 and 750 K (Fig. 7b) temperature range. This low thermal conductivity is a consequence of anisotropic thermal vibration of copper atoms especially Cu2 and Cu3 in the structure as observed in the high temperature orthorhombic phase, which effectively scatters phonons. Indeed recent calculation indicated shorter mean free path of phonons for the high temperature phase compared to the low temperature phase [40]. This remarkably low total thermal conductivity is comparable to the recently discovered Cu-containing high *zT* materials, Cu$_{11}$ZnSb$_4$S$_{13}$ and Cu$_{10}$Ni$_2$Sb$_4$S$_{13}$ [10,11] but lower than many other high *zT* Cu-containing ternary and quaternary chalcogenides [1–9].

3.6. Band structure calculation

The electronic band structure calculations for monoclinic and disordered orthorhombic Cu$_4$SnS$_4$ were performed within sX-LDA method to correct the known failure of the local density approximation to describe band gaps in semiconductors. Indeed, in contrast to prior theoretical PBE-based work [52] where zero-gap and a gap of 0.39 eV have been obtained for monoclinic and ordered orthorhombic Cu$_4$SnS$_4$, respectively, we find the band gap of 0.74 eV and 0.49 eV for monoclinic and disordered orthorhombic Cu$_4$SnS$_4$, respectively. In both
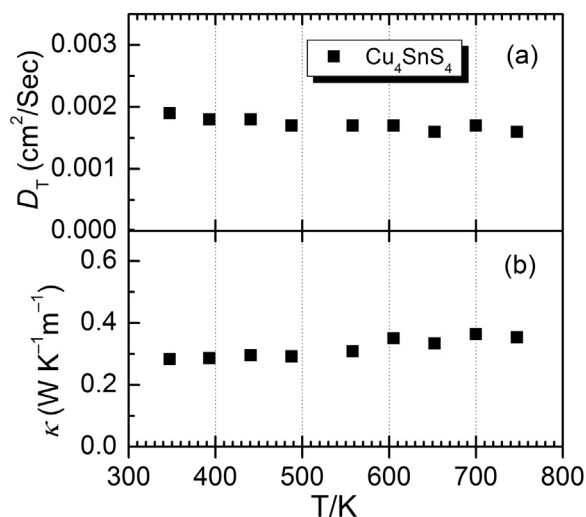

Fig. 6. Temperature dependence (16 – 350 K) of electrical resistivity, ρ (top) and Seebeck coefficient, α (bottom) for Cu$_4$SnS$_4$ sample.

Fig. 7. Temperature dependence of (a) thermal diffusivity (D$_T$) and (b) total thermal conductivity (κ) of Cu$_4$SnS$_4$.
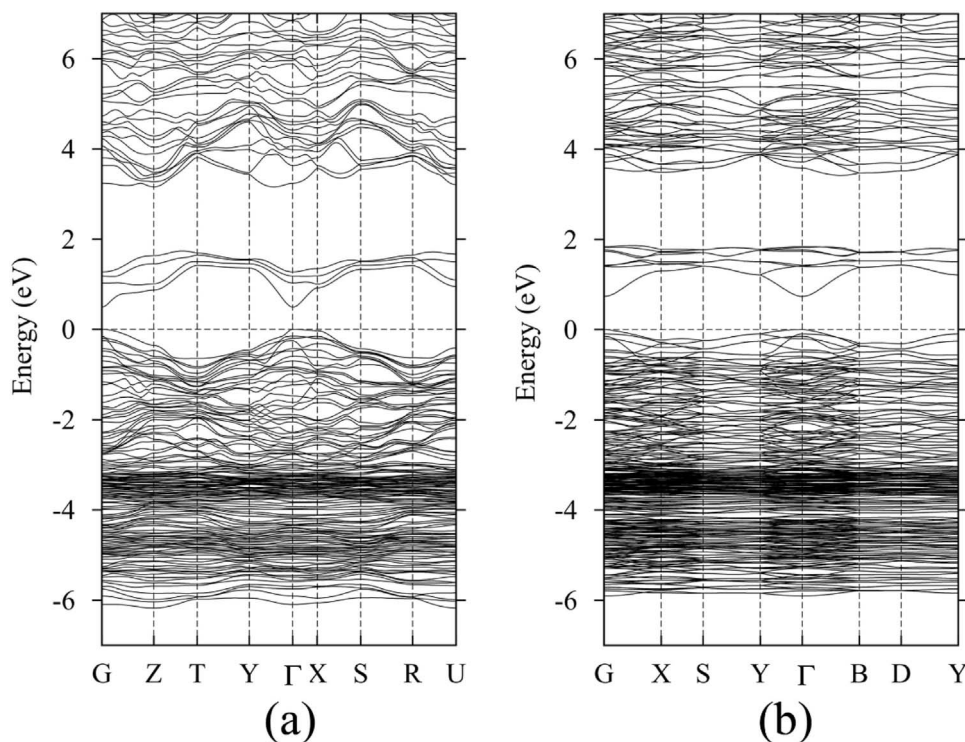
Fig. 8. The theoretical band structures of (a) room temperature orthorhombic and (b) low temperature monoclinic phase of Cu_4SnS_4. The Fermi level is at 0 eV.

phases, the band gap is direct, at Γ point, Fig. 8, which is in agreement with our experimental DRS observations. In agreement with previous calculations [52], we find that the valence band of Cu_4SnS_4 is formed from Cu-$3d$ and S-$3p$ states, whereas the bottom of the conduction band is formed from strongly hybridized Sn-$5s$ and S-$3p$ states. As mentioned earlier, the results of ^{119}Sn Mössbauer analysis indicate that the sulfide coordination environment around tin centers are nearly identical in the monoclinic and room temperature orthorhombic phases. This provides us with the very important insight that the conduction band structure and energy levels are probably not affected extensively as the monoclinic phase is transforming into the orthorhombic phase in agreement with the similar electron effective masses calculated for both phases (see below). However, as one can take cue from crystal structures, the phase transformation follows the significant copper ions movement which causes an unavoidable change in the Cu − S coordination environment. The stronger distortions in the Cu − S polyhedra in the monoclinic phase as compared to the orthorhombic phase reduce the overlap between the Cu-$3d$ and S-$3p$ orbitals which both contribute to the construction of the valence band. As a consequence of the suppressed hybridization, the corresponding bands are flat in the monoclinic phase in comparison to the dispersed valence bands in the orthorhombic phase, Fig. 8. The narrower bandwidth of the valence band leads to a larger band gap in the monoclinic Cu_4SnS_4 in comparison to the orthorhombic phase. On the other hand, the reduced band gap of the orthorhombic phase is likely to be responsible for the increased conductivity by making intrinsic defects to be easily activated. Also note that both phases feature the second gap of about 1.5 eV, Fig. 8, with the second conduction band formed by the empty 5p states of the Sn cations. The second conduction band is expected to appear in the absorption spectra above 3.5 eV. The electrical and thermal properties, however, are governed by the states in the valence and the first conduction bands only.

The bottom of the conduction band in Cu_4SnS_4 is parabolic in both phases, Fig. 8. Indeed, the calculated electron effective masses are similar and nearly isotropic: 0.72 m_e for the $\Gamma\rightarrow$X and $\Gamma\rightarrow$Y directions and 0.75 m_e for the $\Gamma\rightarrow$B direction in the monoclinic phase; and 0.72 m_e for $\Gamma\rightarrow$Z, 0.60 m_e for $\Gamma\rightarrow$Y, and 0.67 m_e for the $\Gamma\rightarrow$X direction in the

orthorhombic phase. In marked contrast, the hole effective masses are highly anisotropic: 1.56 m_e for $\Gamma\rightarrow$X, 6.75 m_e for $\Gamma\rightarrow$Y, and 1.38 m_e for the $\Gamma\rightarrow$B direction in monoclinic phase; and 6.36 m_e for $\Gamma\rightarrow$Z, 0.63 m_e for $\Gamma\rightarrow$Y, and 16.54 m_e for the $\Gamma\rightarrow$X direction in orthorhombic phase. Such low hole effective mass in the $\Gamma\rightarrow$Y direction in the orthorhombic phase may contribute to the observed increase in the conductivity upon the **LT-HT** transition, Fig. 6. We note, that the disordered nature of the orthorhombic phase is likely to favor cation antisite defects such as Cu_{Sn} (n-type) or Sn_{Cu} (p-type) and, therefore, may affect the carrier generation and transport in undoped Cu_4SnS_4. Calculations of the formation energy of these and other intrinsic defects (e.g., S interstitial, S_i, and Sn vacancy, V_{Sn} etc) are beyond the scope of this work and will be presented elsewhere.

3.7. Electrochemical lithium insertion

As mentioned in the structural description section only 5/8 of the tetrahedral holes are occupied by the cations (Sn and Cu) and all the octahedral holes are empty. This allows one to do intercalation chemistry through reductive (Sn^{4+} to Sn^{2+}) insertion of lithium ion either chemically or electrochemically. If lithium can be inserted electrochemically in a reversible manner with concomitant reduction of Sn^{4+} to Sn^{2+}, then the compound can act as an electrode material for Li-ion battery. Based on two electron process, $Cu_4Sn^{IV}S_4 \rightarrow Li_2Cu_4Sn^{II}S_4$, a theoretical capacity of 106.96 mAh/g can be achieved. Initial efforts to insert two electrons in the voltage range 2.8 − 0.5, in C/50 rate lead to an experimental capacity of 449.83 mAh/g, which is in excess of the theoretical capacity based on a 2e process. However, this process is not reversible which may indicate that setting the lower cut-off voltage to 0.5 V leads to reduction of Cu^{1+} to Cu^0 or Sn^{4+} to Sn^0. But when the voltage range for the charge-discharge was set to 1.8 − 3.5 volt, a reversible process is observed in C/50 rate achieving a capacity of 53.48 mAh/g, which only accounts for one Li-ion insertion leading to mixed valence composition of Sn, $LiCu_4Sn^{ii/iv}S_4$, if a topotactic intercalation mechanism is assumed. The voltage-composition profile during the first discharge starts at the open circuit potential (OCP) of 3.17 V which decreases monotonically, suggesting solid-
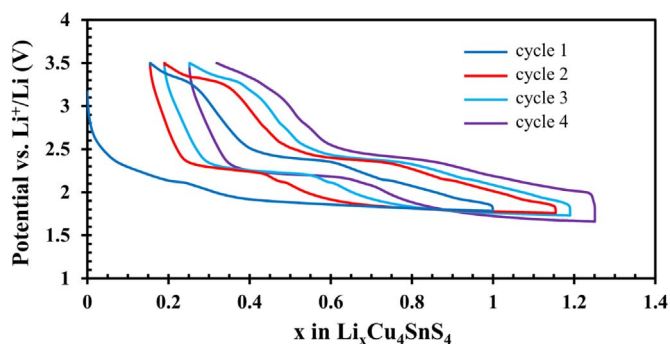
Fig. 9. Voltage-composition charge-discharge curves for lithium reaction with Cu_4SnS_4.

solution formation between the redox phases (Fig. 9). Further reductive insertion of Li^+ leads to the appearance of small flat regions and a large plateau at 2.12 and 1.94 V, respectively, indicating the occurrence of multiple phase transformations. Starting from the second cycle, the voltage-composition profile exhibits a fast decrease until insertion of 0.1 Li^+ per formula unit, after which a flat profile can be observed up to insertion of 0.3 Li^+ ions at 2.22 V. Further discharge accompanies with the appearance of the second flat profile at 1.90 V up to the end of the discharge cycle. Unlike the discharge curves, the charge voltage-composition profiles demonstrate at least three plateaus, evidencing several phase transformations during oxidative delithiation. Consecutive cycling suggests that the specific capacity remains stable which is an indication of acceptable reversibility of the redox system. However, the amount of active electrode materials in the cell (~3 mg) was too small for characterization using Mössbauer or X-ray to determine the change in oxidation state of Sn or structural stability due to reaction with lithium, respectively. Therefore, it was not possible to conclude whether a conversion or an intercalative mechanism of lithium reaction was taking place.

4. Conclusions

Through this work we have shown that Cu_4SnS_4 undergoes a phase transition from an ordered monoclinic phase to a disordered orthorhombic phase at 232 K. The facile movement of the copper ions in the high temperature phase is responsible for the phase transition and the chemical environment of Sn in the lattice remains unchanged as seen through the Mössbauer spectroscopy. Cu_4SnS_4 is direct band gap material as evident from the experimental band gap determination and theoretical calculation of the electronic band structure. The larger band gap in low temperature monoclinic phase has been attributed to narrower valence band due to reduced hybridization between the Cu-*3d* and S-*3p* orbitals. The cause of higher conductivity in the orthorhombic phase can be attributed to the reduced band gap leading to facile activation of the defects as well as low hole effective mass in one of the crystallographic directions. Cu_4SnS_4 is also electrochemically active in reversible Li-insertion, however, exact mechanism (topotactic or conversion) is still unclear.

Acknowledgements

Appendix A. Supporting information

Supplementary data associated with this article can be found in the online version at doi:10.1016/j.jssc.2017.05.033.

References

[1] X.Y. Shi, F.Q. Huang, M.L. Liu, L.D. Chen, Appl. Phys. Lett. 94 (2009) 122103.
[2] M.L. Liu, F.Q. Huang, L.D. Chen, I.W. Chen, Appl. Phys. Lett. 94 (2009) 202103.
[3] M.L. Liu, I.W. Chen, F.Q. Huang, L.D. Chen, Adv. Mater. 21 (2009) 3808–3812.
[4] X.Y. Shi, L.L. Xi, J. Fan, W.Q. Zhang, L.D. Chen, Chem. Mater. 22 (2010) 6029–6031.
[5] J.Y. Cho, X. Shi, J.R. Salvador, G.P. Meisner, J. Yang, H. Wang, A.A. Wereszczak, X. Zhou, C. Uher, Phys. Rev. B 84 (2011) 085207.
[6] E.J. Skoug, J.D. Cain, D.T. Morelli, Appl. Phys. Lett. 98 (2011) 261911.
[7] T. Plirdpring, K. Kurosaki, A. Kosuga, T. Day, S. Firdosy, V. Ravi, G.J. Snyder, A. Harnwunggmoung, T. Sugahara, Y. Ohishi, H. Muta, S. Yamanaka, Adv. Mater. 24 (2012) 3622–3626.
[8] R. Liu, L. Xi, H. Liu, X. Shi, W. Zhang, L. Chen, Chem. Commun. 48 (2012) 3818–3820.
[9] H. Liu, X. Shi, F. Xu, L. Zhang, W. Zhang, L. Chen, Q. Li, C. Uher, T. Day, G.J. Snyder, Nat. Mater. 11 (2012) 422–425.
[10] X. Lu, D.T. Morelli, Y. Xia, F. Zhou, V. Ozolins, H. Chi, X.Y. Zhou, C. Uher, Adv. Energy Mater. 3 (2013) 342–348.
[11] K. Suekuni, K. Tsuruta, M. Kunii, H. Nishiate, E. Nishibori, S. Maki, M. Ohta, A. Yamamoto, M. Koyano, J. Appl. Phys. 113 (2013) 043712.
[12] K.S. Weldert, W.G. Zeier, T.W. Day, M. Panthöfer, G.J. Snyder, W. Tremel, J. Am. Chem. Soc. 136 (2014) 12035–12040.
[13] Y. He, T. Zhang, X. Shi, S.-H. Wei, L. Chen, NPG Asia Mater. 7 (2015) e210.
[14] H. Katagiri, K. Jimbo, W.S. Maw, K. Oishi, M. Yamazaki, H. Araki, A. Takeuchi, Thin Solid Films 517 (2009) 2455–2460.
[15] T.A. Kuku, O.A. Fakolujo, Sol. Energ. Mater. 16 (1987) 199–204.
[16] M.G. Panthani, V. Akhavan, B. Goodfellow, J.P. Schmidtke, L. Dunn, A. Dodabalapur, P.F. Barbara, B.A. Korgel, J. Am. Chem. Soc. 130 (2008) 16770–16777.
[17] M.A. Contreras, B. Egaas, K. Ramanathan, J. Hiltner, A. Swartzlander, F. Hasoon, R. Noufi, Prog. Photovolt. Res. Appl. 7 (1999) 311–316.
[18] Q. Guo, G.M. Ford, W.-C. Yang, B.C. Walker, E.A. Stach, H.W. Hillhouse, R. Agrawal, J. Am. Chem. Soc. 132 (2010) 17384–17386.
[19] D.B. Mitzi, O. Gunawan, T.K. Todorov, K. Wang, S. Guha, Sol. Energy Mater. Sol. Cells 95 (2011) 1421–1436.
[20] Q. Guo, H.W. Hillhouse, R. Agrawal, J. Am. Chem. Soc. 131 (2011) 11672–11673.
[21] C. Steinhagen, M.G. Panthani, V. Akhavan, B. Goodfellow, B. Koo, B.A. Korgel, J. Am. Chem. Soc. 131 (2011) 12554–12555.
[22] S.C. Riha, B.A. Parkinson, A.L. Prieto, J. Am. Chem. Soc. 131 (2009) 12054–12055.
[23] A. Shavel, J. Arbiol, A. Cabot, J. Am. Chem. Soc. 132 (2010) 4514–4515.
[24] S. Bag, O. Gunawan, T. Gokmen, Y. Zhu, T.K. Todorov, D.B. Mitzi, Energy Environ. Sci. 5 (2012) 7060–7065.
[25] P. Jackson, D. Hariskos, E. Lotter, S. Paetel, R. Wuerz, R. Menner, W. Wischmann, M. Powalla, Prog. Photovolt.: Res. Appl. 19 (2011) 894–897.
[26] M.G. Panthani, V. Akhavan, B. Goodfellow, J.P. Schmidtke, L. Dunn, A. Dodabalapur, P.F. Barbara, B.A. Korgel, (B. A)J. Am. Chem. Soc. 130 (2008) 16770–16777.
[27] D. Tiwari, T.K. Chaudhuri, T. Shripathi, U. Deshpande, R. Rawat, Sol. Energy Mater. Sol. Cells 113 (2013) 165–170.
[28] P. Zawadzki, L.L. Baranowski, H. Peng, E.S. Toberer, D.S. Ginley, W. Tumas, A. Zakutayev, S. Lany, Appl. Phys. Lett. 103 (2013) 253902.
[29] L.L. Baranowski, P. Zawadzki, S. Christensen, D. Nordlund, S. Lany, A.C. Tamboli, L. Gedvilas, D.S. Ginley, W. Tumas, E.S. Toberer, A. Zakutayev, Chem. Mater. 26 (2014) 4951–4959.
[30] J.-J. Wang, P. Liu, C.C. Seaton, K.M. Ryan, J. Am. Chem. Soc. 136 (2014) 7954–7960.
[31] J. Wang, A. Singh, P. Liu, S. Singh, C. Coughlan, Y. Guo, K.M. Ryan, J. Am. Chem. Soc. 135 (2013) 7835–7838.
[32] M. Ahmadi, S.S. Pramana, S.K. Batabyal, C. Boothroyd, S.G. Mhaisalkar, Y.M. Lam, Inorg. Chem. 52 (2013) 1722–1728.
[33] M. Ibáñez, D. Cadavid, U. Anselmi-Tamburini, R. Zamani, S. Gorsse, W. Li, A.M. López, J.R. Morante, J. Arbiol, A. Cabot, J. Mater. Chem. A 1 (2013) 1421–1426.
[34] J. Fan, W. Carrillo-Cabrera, L. Akselrud, I. Antonyshyn, L. Chen, Y. Grin, Inorg. Chem. 52 (2013) 11067–11074.
[35] M.I. Aliev, D.G. Arasly, T.G. Dzhabrailov, Sov. Phys. Solid State 25 (1983) 2009.
[36] M. Matoba, I. Inoue, T. Uemura, M. Watanabe, S. Anzai, Zair. Kagaku (J. Mater. Sci. Soc. Jpn.) 27 (1990) 299–301.
[37] S. Kondo, M. Hasaka, T. Morimura, International Conference on Thermoelectrics, ICT, Proceedings, pp. 238–242, 1996.

[38] M. Hasaka, T. Aki, T. Morimura, S.-I. Kondo, Energ. Convers. Manag. 38 (1997) 855–859.

[39] Y. Goto, Y. Kamihara, M. Matoba, J. Electron Mater. 43 (2014) 2202–2205.

[40] A. Suzumura, N. Nagasako, Y. Kinoshita, M. Watanabe, T. Kita, R. Asahi, Mater. Trans. 56 (2015) 858–863.

[41] Q. Chen, X. Dou, Z. Li, Y. Ni, J. Chen, F. Zhou, Y. Yamaguchi, S. Zhuang, Optik 125 (2014) 3217–3220.

[42] M. Khanafer, J. Rivet, J. Flahaut, Bull. Soc. Chim. Fr. (1974) 2670–2776.

[43] M. Khanafer, O. Gorochov, J. Rivet, Mater. Res. Bull. 9 (1974) 1543–1552.

[44] S. Anzai, K. Ozawa, JAERI-M reports 1 (1984) 84 − 0591.

[45] K. Ozawa, S. Anzai, S. Minomura (Ed.)Solid State Physics Under Pressure, Terra Scientific Publishing Company, 1985, pp. 269–274.

[46] S. Anzai, F. Tadahiro, J. Phys. Soc. Jpn. 55 (1986) 701–702.

[47] S. Anzai, I. Inoue, M. Matoba, T. Kamimura, Rep. Asahi Glass Found. 57 (1990) 229–230.

[48] S. Anzai, M. Matoba, I. Inoue, T. Fukazawa, T. Kamimura, K. Kitamura, J. Phys. Soc. Jpn. 59 (1990) 3799–3800.

[49] T. Kamimura, M. Matoba, S. Anzai, J. Phys. Soc. Jpn. 59 (1990) 3045–3048.

[50] P.S. Jaulmes, J. Rivet, P. Laruelle, Acta Crystallogr. B 33 (1977) 540–542.

[51] J. Mahy, J. Van Landuyt, S. Amelinckx, Solid State Commun. 54 (1985) 621–624.

[52] Y. Goto, Y. Kamihara, M. Matoba, Phys. Status Solidi C Curr. Top. Solid State Phys. 10 (2013) 1127–1129.

[53] Bruker AXS Inc., SMART, Madison, Wisconsin, USA (2002).

[54] Bruker AXS Inc., SAINT and SADABS, Madison, Wisconsin, USA (2008).

[55] W. Herrendorf, Habitus, A Program for the Optimization of the Crystal Shape for Numerical Absorption Correction, University of Gießen: Gießen, Germany, 1995.

[56] G.M. Sheldrick, Acta Crystallogr. A64 (2008) 112–122.

[57] V. Petříček, M. Dusek, L. Palatinus, Z. Krist. 229 (2014) 345–352.

[58] X.-A. Chen, M. Onoda, H. Wada, A. Sato, H. Nozaki, R. Herbst-Irmer, J. Solid State Chem. 145 (1999) 204–211.

[59] P. Kubelka, F.Z. Munk, Technol. Phys. 12 (1931) 593–601.

[60] G. Kotum, Reflectance Spectroscopy, Springer-Verlag, New York, 1969.

[61] E. Wimmer, H. Krakauer, M. Weinert, A.J. Freeman, Phys. Rev. B 24 (1981) 864–875.

[62] M. Weinert, E. Wimmer, A.J. Freeman, Phys. Rev. B 26 (1982) 4571–4578.

[63] R. Asahi, W. Mannstadt, A.J. Freeman, Phys. Rev. B 59 (1999) 7486–7492.

[64] M.Y. Kim, R. Asahi, A.J. Freeman, J. Comput.-Aided Mater. Des. 9 (2002) 173–201.

[65] C.B. Geller, W. Wolf, S. Picozzi, A. Continenza, R. Asahi, W. Mannstadt, A.J. Freeman, E. Wimmer, Appl. Phys. Lett. 79 (2001) 368–370.

[66] A. Murat, J.E. Medvedeva, Phys. Rev. B 85 (2012) 155101.

[67] M. Kim, Y.J. Zhao, A.J. Freeman, W. Mannstadt, Appl. Phys. Lett. 84 (2004) 3579–3581.

[68] X.-A. Chen, H. Wada, A. Sato, M. Mieno, J. Solid State Chem. 139 (1998) 144–151.

[69] F. Di Benedetto, G.P. Bernardini, D. Borrini, W. Lottermoser, G. Tippelt, G. Amthauer, Phys. Chem. Miner. 31 (2005) 683–690.

[70] J.H. Liao, M.G. Kanatzidis, Chem. Mater. 5 (1993) 1561–1569.

[71] D. Avellaneda, M.T.S. Nair, P.K. Nair, J. Electrochem. Soc. 157 (2010) D346–D352.